Organic Cation Alloying on Intralayer A and Interlayer A' sites in 2D Hybrid Dion-Jacobson Lead Bromide Perovskites (A')(A)Pb2Br7

Lingling Mao, Peijun Guo, Mikael Kepenekian, Ioannis Spanopoulos, Yihui He, Claudine Katan, Jacky Even, Richard Schaller, Ram Seshadri, Constantinos C Stoumpos, et al.

▶ **To cite this version:**

Lingling Mao, Peijun Guo, Mikael Kepenekian, Ioannis Spanopoulos, Yihui He, et al.. Organic Cation Alloying on Intralayer A and Interlayer A' sites in 2D Hybrid Dion-Jacobson Lead Bromide Perovskites (A')(A)Pb2Br7. Journal of the American Chemical Society, 2020, 142 (18), pp.8342-8351. 10.1021/jacs.0c01625 . hal-02540856

HAL Id: hal-02540856
https://hal.science/hal-02540856

Submitted on 19 May 2020

HAL is a multi-disciplinary open access archive for the deposit and dissemination of scientific research documents, whether they are published or not. The documents may come from teaching and research institutions in France or abroad, or from public or private research centers.

L'archive ouverte pluridisciplinaire **HAL**, est destinée au dépôt et à la diffusion de documents scientifiques de niveau recherche, publiés ou non, émanant des établissements d'enseignement et de recherche français ou étrangers, des laboratoires publics ou privés.

Organic Cation Alloying on Intralayer A and Interlayer A' sites in 2D Hybrid Dion-Jacobson Lead Bromide Perovskites (A')(A)Pb_2Br_7

Lingling Mao[1,2], Peijun Guo[3], Mikaël Kepenekian[4], Ioannis Spanopoulos[1], Yihui He[1], Claudine Katan[4], Jacky Even[5], Richard D. Schaller[1,3], Ram Seshadri[2], Constantinos C. Stoumpos[1*], and Mercouri G. Kanatzidis[1*]

[1]Department of Chemistry, Northwestern University, 2145 Sheridan Road, Evanston, Illinois 60208, United States

[2] Materials Department and Materials Research Laboratory, Department of Chemistry and Biochemistry, University of California, Santa Barbara, California 93106, United States

[3]Center for Nanoscale Materials, Argonne National Laboratory, 9700 South Cass Avenue, Lemont, Illinois 60439, United States

[4]Univ Rennes, ENSCR, INSA Rennes, CNRS, ISCR (Institut des Sciences Chimiques de Rennes) – UMR 6226, Rennes F-35000, France

[5]Univ Rennes, INSA Rennes, CNRS, Institut FOTON – UMR 6082, Rennes F-35000, France

Supporting Information Placeholder

ABSTRACT: Hybrid layered halide perovskites have achieved impressive performance in optoelectronics. New structural types in the two-dimensional (2D) halide system such as the Dion-Jacobson phases have attracted wide research attention due to the short interlayer distance and unique layer orientation that facilitate better charge-transport and higher stability in optoelectronic devices. Here, we report the first solid solution series incorporating both A and A' cations in the 2D Jacobson-Dion family, with the general formula (A')(A)Pb_2Br_7 ((A' = 3-(aminomethyl)piperidinium (3AMP) and 4-(aminomethyl)piperidinium) (4AMP); A= methylammonium (MA) and formamidinium (FA)). Mixing the spacing A' cations and perovskitizer A cations generates the new $(3AMP)_a(4AMP)_{1-a}(FA)_b(MA)_{1-b}Pb_2Br_7$ perovskites. The crystallographically refined crystal structures using single-crystal X-ray diffraction data reveal that the distortion of the inorganic framework is heavily influenced by the degree of A' and A alloying. A rising fraction of 4AMP in the structure, decreases the Pb-Br-Pb angles, making the framework more distorted. On the contrary, higher FA fractions increase the Pb-Br-Pb angles. This structural evolution fine tunes the optical properties where the larger the Pb-Br-Pb angle, the narrower the band gap. The photoluminescence emission energy mirrors this trend. Raman spectroscopy reveals a highly dynamical lattice similar to $MAPbBr_3$ and consistent with the local distortion environment of the [Pb_2Br_7] framework. Density Functional Theory (DFT) calculations of the electronic structures reveal the same trend as the experimental results where (3AMP)(FA)Pb_2Br_7 has the smallest band gap while (4AMP)(MA)Pb_2Br_7 has the largest band gap. The structural effects from solely the organic cations in the 2D system highlight the importance of understanding the high sensitivity of the optoelectronic properties on the structural tuning in this broad class of materials.

INTRODUCTION

Hybrid organic-inorganic halide perovskite materials have established themselves as one of the leading semiconducting materials because of their superior performances in optoelectronics.[1-4] The ease of thin-film preparation and favorable properties of the hybrid perovskites such as long carrier diffusion length, long carrier lifetime, high carrier mobility and optimal absorption properties are helping to elevate the performance even better, currently up to 25.2% power conversion efficiency (PCE).[5] Substituting the iodide with bromide increases the band gap of the hybrid perovskite materials, making them more suitable for tandem solar cells[6,7] and green LEDs.[8-12] Breakthroughs with perovskite-based materials have also been reported recently in light emitting diodes (LEDs), where the highest external quantum efficiency (EQE) has reached 20%.[13] A recent strategy for fabricating high performance photovoltaic devices is to mix various of A-site cations (Cs^+, FA^+, MA^+) that boosts the performance compared to the pristine samples.[7,14-16] This performance boost is achieved mainly from an increased charge-carrier mobility,[17] which generally connects with the fine crystal structure details of the perovskite. Other chemical strategies that aid device performance involve composition tuning with halide-mixing and incorporating additives in the thin-films.[18-20] In most cases, despite the PCE improvement, structural details and insights were not provided, mainly because of complications from the dynamical disorder in the 3D systems.[21-23]

The 2D hybrid perovskites expand the range of properties and possibilities because of their highly diverse chemistry,[24-30]

Accepted Manuscript

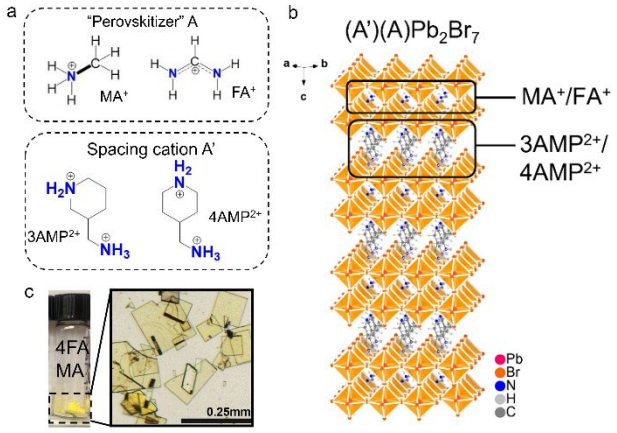

Figure 1. (a) Structures of the "perovskitizer" (MA^+ and FA^+) and spacing cation ($3AMP^{2+}$ and $4AMP^{2+}$) (Blue: nitrogen, dark grey: carbon, light grey: hydrogen). (b) General crystal structure of $(A')(A)Pb_2Br_7$ incorporating both mixed A cation (MA^+/FA^+) and mixed A' cation ($3AMP^{2+}/4AMP^{2+}$). (c) Picture of an example of the resulting 2D compounds, $(4AMP)(FA)_{0.5}(MA)_{0.5}Pb_2Br_7$.

excellent photo-physical properties[31,32], and intriguing physical phenomena such as electron/exciton-phonon coupling[33] and Rashba splitting[34] for spintronics.[35-37] The reduction in dimensionality from 3D to 2D lends additional flexibility to the crystal lattice and as a result, the tolerance factor limitation that occurs in the 3D perovskite can be somewhat relaxed in 2D perovskite.[38,39] Typical examples are the 2D perovskites which based on the tolerance-"forbidden" cations ethylammonium (EA)[28,40], isopropylammonium (IPA)[41] and a series of larger A-site cations.[42] An added important benefit of the 2D perovskites is that large organic spacer cations with appropriate functional groups can be inserted between the 2D layers.[43-45] The organic spacer cations engage in various supramolecular interactions such as fluoroaryl-aryl interactions and hydrogen bonding,[46,47] and can exhibit chemical reactivity such as halogen insertion[48] and Diels-Alder cycloaddition.[49] Aside from the diversity of the organic part, the inorganic lattice can adopt different layer orientation (100-oriented,[50,51] 110-oriented[45,52,53] and 111-oriented[54,55] with respect to the ideal cubic perovskite), and layer thickness (n= 1-7).[56-59] Layered double perovskites with alternating 1+ and 3+ metal cations are also reported.[60-63] Moreover, 2D layered perovskites further divide the into two main subcategories, the Ruddlesden–Popper (RP) phases (with 1+ cations)[64] and the Dion–Jacobson (DJ) phases (with 2+ cations),[65] according to the charge of the organic cation and stacking modes of the layers. Several cases of multilayered hybrid lead bromide perovskites have been recently reported, including $(C_4H_9NH_3)_2CsPb_2Br_7$,[66] $(C_4H_9NH_3)_2(NH_2CHNH_2)Pb_2Br_7$,[67] $(C_4H_9NH_3)_2(CH_3NH_3)_2Pb_3Br_{10}$[68] and $[CH_3(CH_2)_3NH_3]_2(CH_3NH_3)Pb_2Br_7$,[69] exhibiting ferroelectric properties.

Herein, we present organic cation mixing in the new family 2D DJ $(A')(A)Pb_2Br_7$ perovskites aiming to reveal the links between the fine-tuning of the structural features and optoelectronic properties. Through controlled mixing of both A-site cation (MA, FA), which we refer to as the "perovskitizer" cations (meaning they template/occupy only the perovskite

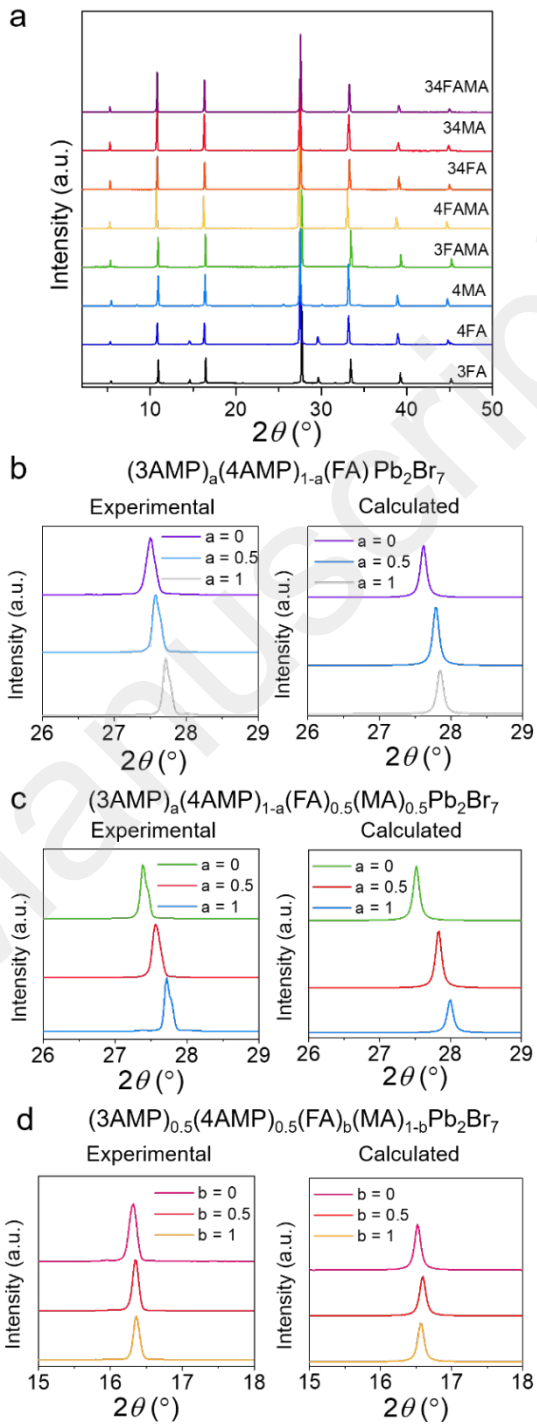

Figure 2. (a) Powder X-ray diffraction (PXRD) patterns of the 2D compounds (labels are abbreviated such as 3FA = $(3AMP)(FA)Pb_2Br_7$, 34FA = $(3AMP)_{0.5}(4AMP)_{0.5}(FA)Pb_2Br_7$) (Cu K$\alpha$ rad). (b-d) Zoom-in regions of both the experimental and calculated PXRD patterns showing the gradual lattice parameter change when introducing a new cation.

cuboctahedral cage), and A'-cation (the large organic spacer), we demonstrate that the degree of distortion of the perovskite in each individual layer can be controlled. We take advantage of the similar size and functionality of the 3AMP and 4AMP cations, to build double solid-solutions composed of both mixed A' and A cations. By combining A' (3AMP/4AMP) and

For Review Only Manuscript

A (MA/ FA), we synthesized nine different compounds based on the (A')(A)Pb_2Br_7 (A' = 3AMP or 4AMP, A = FA or MA) formula. They exhibit distinctive perovskite distortion modes ranging from out-of-phase tilting to in-phase tilting along with the undistorted structural prototype (Figure 1). The powder X-ray diffraction (PXRD) data shows pure phase for each solid solution and small Bragg peak shifts due to the change of the unit cell volume. We determined the inorganic distortion (i.e. the Pb-Br-Pb angles) in the crystal structure using single-crystal X-ray diffraction for selected compositions of the $(3AMP)_a(4AMP)_{1-a}(FA)_b(MA)_{1-b}Pb_2Br_7$ (a and b = 1, 0.5 or 0) system. We find a dependence of the Pb-Br-Pb angles on both a and b variables, with the angle becoming smaller (i.e. larger distortion) with decreasing value of a and b. The optical band gap obeys the general "rule" of the halide perovskites which states that the larger the Pb-Br-Pb angle, the smaller the band gap, which is also seen in the emission energy of the photoluminescence (PL).[70] The compositional mapping employed in this work provides an excellent tool for understanding how subtle changes at the organic cation sites drive the structural evolution within the inorganic layer of a given 2D hybrid halide perovskite, thus acting as synthetic knobs to control the semiconducting properties of the materials.

RESULTS AND DISCUSSION

Synthesis. The synthesis procedure for the two-layered (A')(A)Pb_2Br_7 (A' = 3AMP or 4AMP, A = FA or MA) series of compounds was as previously reported for the iodides,[65] changing only the solvent from hydroiodic acid to hydrobromic acid (see Methods). To synthesize the solid-solutions using mixed cations, the experimental ratios of the A' and A cation was controlled stoichiometrically, e.g. for $(3AMP)_{0.5}(4AMP)_{0.5}(FA)_{0.5}(MA)_{0.5}Pb_2Br_7$, the experimental ratio of 3AMP:4AMP:FA:MA was 1:1:1:1. The resulting compositions of the hybrid compounds are listed in Table S10, which are based on the ^{1}H NMR results.[71] Although the initial input of each component is the same for $(3AMP)_{0.5}(4AMP)_{0.5}(FA)_{0.5}(MA)_{0.5}Pb_2Br_7$, the outcome is slightly different as more 4AMP and MA were incorporated in the compound, which was a general trend seen in the series. The as-synthesized compounds grow as yellow crystals with a thin, rectangular plate-like morphology (Figure 1 and S1).

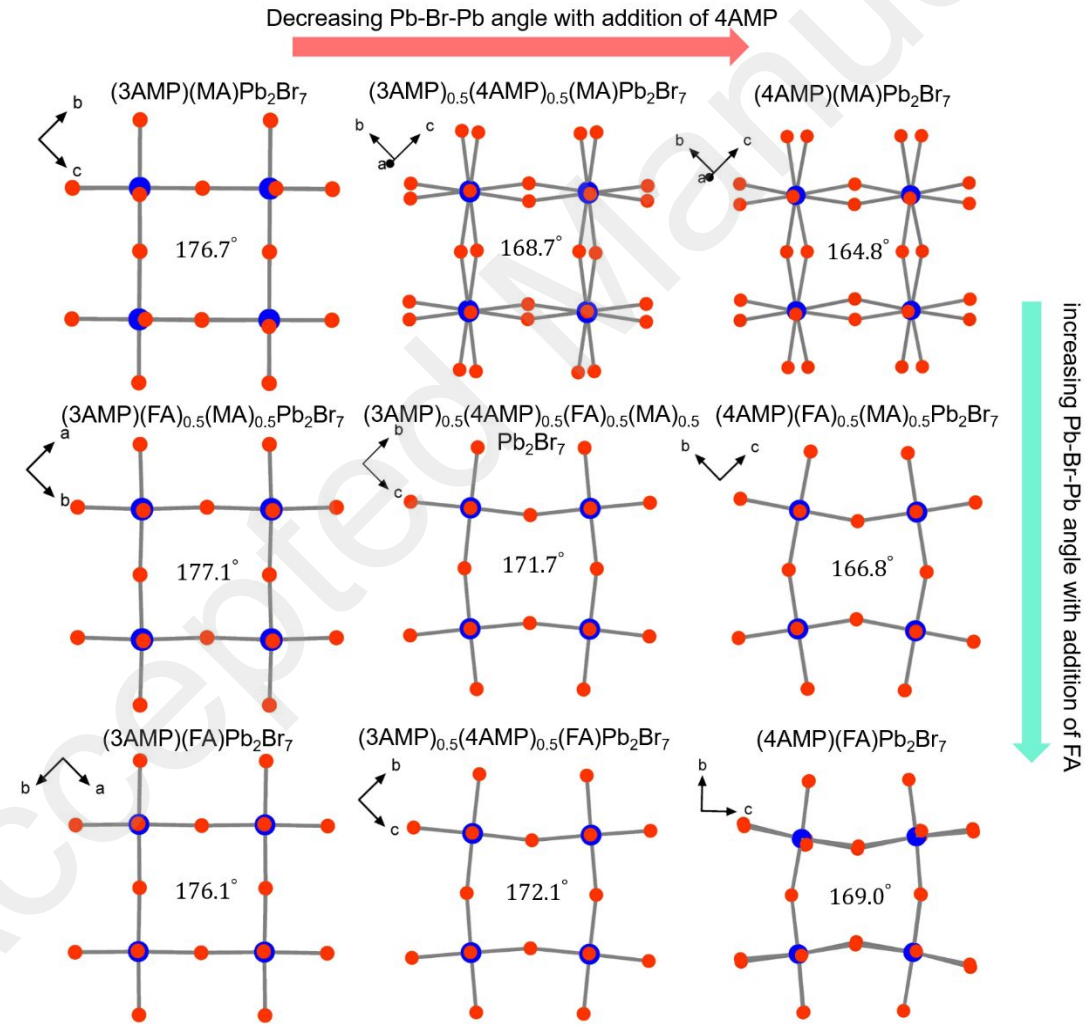

Figure 3. Top-down view of the crystal structure of the nine members of the extended solid solution $(3AMP)_a(4AMP)_{1-a}(FA)_b(MA)_{1-b}Pb_2Br_7$ (a and b = 1, 0.5 or 0). Averaged Pb-Br-Pb angles in the inorganic framework of each composition are labeled. Atom symbol: orange (Br), blue (Pb), organic cations are omitted here for clarity. The nine structures can be generalized in three types of structural modes: α, β and γ. Mode α:3MA, 3FAMA and 3FA. Mode β: 4MA, 34MA. Mode γ: 34FAMA, 4FAMA, 34FA and 4FA.

Accepted Manuscript

Table 1. Crystal data and structure refinement for $(3AMP)_a(4AMP)_{1-a}(FA)_b(MA)_{1-b}Pb_2Br_7$ (a and b = 1, 0.5 or 0).

Compound	$(3AMP)(FA)Pb_2Br_7$	$(3AMP)(MA)Pb_2Br_7$	$(4AMP)(FA)Pb_2Br_7$	$(4AMP)(MA)Pb_2Br_7$
Chemical formula	$(C_6N_2H_{16})[HC(NH_2)_2]Pb_2Br_7$	$(C_6N_2H_{16})(CH_3NH_3)Pb_2Br_7$	$(C_6N_2H_{16})[HC(NH_2)_2]Pb_2Br_7$	$(C_6N_2H_{16})(CH_3NH_3)Pb_2Br_7$
Space group	*Cm*	*Pc*	*Pc*	*Cc*
Unit cell dimensions	a = 8.4615(17) Å, b = 8.4650(17) Å, c = 16.004(3) Å, β = 89.99(3)°	a = 15.952(3) Å, b = 8.4134(17) Å, c = 8.4135(17) Å, β = 90.07(3)°	a = 16.138(3) Å, b = 11.909(2) Å, c = 11.905 (7) Å, β = 90.00(3)°	a = 33.433(7) Å, b = 8.3738(17) Å, c = a8.3760(17) Å, β = 104.45(3)°
Vol (Å³), Z	1146.3(4), 2	1129.2(4), 2	2288.0(8), 4	2270.8(8), 4
ρ (g/cm³)	3.288	3.300	3.295	3.282
Indepd. refl.	3034 [R_{int} = 0.0308]	5582 [R_{int} = 0.1475]	11594 [R_{int} = 0.1533]	3739 [R_{int} = 0.1023]
Data / restr. / param.	3034 / 30 / 75	5582 / 30 / 119	11594 / 55 / 236	3739 / 80 / 117
R indices [I>2σ(I)]	R_{obs} = 0.0460, wR_{obs} = 0.1138	R_{obs} = 0.0897, wR_{obs} = 0.2695	R_{obs} = 0.0633, wR_{obs} = 0.1319	R_{obs} = 0.0795, wR_{obs} = 0.1826

Table 2. Crystal data and structure refinement for $(3AMP)_a(4AMP)_{1-a}(FA)_b(MA)_{1-b}Pb_2Br_7$ (a and b = 1, 0.5 or 0)

Compound	$(3AMP)_{0.5}(4AMP)_{0.5}(FA)_{0.5}(MA)_{0.5}Pb_2Br_7$	$(4AMP)(FA)_{0.5}(MA)_{0.5}Pb_2Br_7$	$(3AMP)(FA)_{0.5}(MA)_{0.5}Pb_2Br_7$	$(3AMP)_{0.5}(4AMP)_{0.5}(FA)Pb_2Br_7$	$(3AMP)_{0.5}(4AMP)_{0.5}(MA)Pb_2Br_7$
Chemical formula	$(C_6N_2H_{16})[HC(NH_2)]_{2\,0.5}(CH_3NH_3)_{0.5}Pb_2Br_7$	$(C_6N_2H_{16})[HC(NH_2)]_{2\,0.5}(CH_3NH_3)_{0.5}Pb_2Br_7$	$(C_6N_2H_{16})[HC(NH_2)]_{2\,0.5}(CH_3NH_3)_{0.5}Pb_2Br_7$	$(C_6N_2H_{16})[HC(NH_2)_2]Pb_2Br_7$	$(C_6N_2H_{16})(CH_3NH_3)Pb_2Br_7$
Space group	*Pc*	*Pc*	*C2*	*Pc*	*Cc*
Unit cell dimensions	a = 16.0142(12) Å, b = 8.4185(7) Å, c = 8.4164(6) Å, β = 90.024(3)°	a = 16.193(2) Å, b = 8.3678(11) Å, c = 8.3469(10) Å, β = 89.921(6)°	a = 8.4121(8) Å, b = 8.4176(9) Å, c = 15.9228(19) Å, β = 89.983(4)°	a = 16.0382(13) Å, b = 8.4484(7) Å, c = 8.4494(6) Å, β = 89.9940(15)°	a = 33.2368(17) Å, b = 8.3841(5) Å, c = 8.3801(4) Å, β = 104.599(2)°
Vol (Å³), Z	1134.66(15), 2	1131.0(3), 2	1127.5(2), 2	1144.87(16), 2	2259.8(2), 4
ρ (g/cm³)	3.372	3.295	3.346	3.293	3.2977
Indepd. refl.	5492 [R_{int} = 0.0537]	5029 [R_{int} = 0.0436]	2707 [R_{int} = 0.0365]	5599 [R_{int} = 0.0510]	5412 [R_{int} = 0.0542]
Data / restr. / param.	5492 / 27 / 119	5029 / 27 / 118	2707 / 20 / 65	5599 / 29 / 119	5412 / 28 / 118
R indices [I>2σ(I)]	R_{obs} = 0.0448, wR_{obs} = 0.1400	R_{obs} = 0.0576, wR_{obs} = 0.1690	R_{obs} = 0.0443, wR_{obs} = 0.1365	R_{obs} = 0.0505, wR_{obs} = 0.1528	R_{obs} = 0.0461, wR_{obs} = 0.1348

Using powder X-ray diffraction (PXRD), we were able to confirm the compositional purity of the compounds, with all of them exhibiting the characteristic diffraction pattern of the bi-layered perovskite (Figure 2a), in excellent agreement with the calculated ones. Because $(3AMP)(MA)Pb_2Br_7$ decomposes relatively quickly, we could perform only single-crystal XRD analysis. The PXRD patterns of the compounds have the trademark characteristics of a solid-solution with no new peaks emerging showing only a slight peak shift. Considering the 15° and 30° peaks in 3FA and 4FA, they obviously exist

Accepted Manuscript

Table 3. Detailed Pb-Br-Pb (deg) angles solved from the crystal structures and band gap of the nine compounds with the formula (A')(A)Pb_2Br_7 (A' = 3AMP or 4AMP, A = FA or MA).

Compound	Abbreviation	Averaged horizontal Pb-Br-Pb angle	Averaged axial Pb-Br-Pb angle	Average Pb-Br-Pb angle	E_g (eV)	PL (eV)
$(4AMP)(MA)Pb_2Br_7$	4MA	159.9	174.6	164.8	2.82	NA
$(4AMP)(FA)_{0.5}(MA)_{0.5}Pb_2Br_7$	4FAMA	160.2	179.8	166.8	2.81	2.48
$(4AMP)(FA)Pb_2Br_7$	4FA	163.9	179.3	169.0	2.78	2.34
$(3AMP)_{0.5}$ $(4AMP)_{0.5}$ $(MA)Pb_2Br_7$	34MA	163.2	179.6	168.7	2.73	2.42
$(3AMP)_{0.5}$ $(4AMP)_{0.5}(FA)_{0.5}(MA)_{0.5}Pb_2Br_7$	34FAMA	167.7	179.8	171.7	2.73	2.34
$(3AMP)_{0.5}$ $(4AMP)_{0.5}(FA)Pb_2Br_7$	34FA	169.3	177.7	172.1	2.73	2.39
$(3AMP)(MA)Pb_2Br_7$	3MA	178.2	173.5	176.6	NA	NA
$(3AMP)(FA)_{0.5}(MA)_{0.5}Pb_2Br_7$	3FAMA	176.8	177.6	177.1	2.66	2.31
$(3AMP)(FA)Pb_2Br_7$	3FA	176.5	175.4	176.1	2.69	2.30

in every compound since they correspond to the (110) and (220) diffraction planes. The difference in intensity is due to preferred orientation (See Figure S1). Typically, 2D perovskite plate crystals exhibit strong preferred orientation along the [100] direction of the plates, exhibiting mainly the (200), (400), (600)...(*h*00) reflections in the PXRD pattern as seen in Figure 2a.

Crystal structure. To evaluate the effect of the addition of A' and A cations, we group the patterns in three triads (Figure 2b-2d). The first triad, groups the $(3AMP)_a(4AMP)_{1-a}(FA)Pb_2Br_7$ series, where the (10 0 0) peak shifts to lower diffraction angle with increasing amount of 4AMP. This trend matches with the long axis expansion (perpendicular to the layers) determined by single-crystal X-ray diffraction, which the long axes for 3FA, 34FA and 4FA (3FA = (3AMP)(MA) Pb_2Br_7, 34 FA = $(3AMP)_{0.5}(4AMP)_{0.5}(FA)$ Pb_2Br_7, 4FA = (4AMP)(FA)Pb_2Br_7) having values of 16.004(3) Å, 16.0382(13) Å, 16.138(3) Å, respectively. Similarly, in the $(3AMP)_a(4AMP)_{1-a}(FA)_{0.5}(MA)_{0.5}Pb_2Br_7$ series, the peak shifts to lower angles, correspond to the long axis expansion in the (3FAMA (15.923(2) Å) <34FAMA (16.0142(12) Å) <4FAMA (16.193(2) Å) order. Finally, for the $(3AMP)_{0.5}(4AMP)_{0.5}(FA)_b(MA)_{1-b}Pb_2Br_7$ series, the change of the shift becomes much less severe, as the change in the unit cell is much smaller, with the long axis expansion following the 34MA<34FAMA<34MA order having values of 16.0382(13), 16.0142 (12) and 16.082 (transformed),[72] respectively. The pronounced lattice expansion reveals the accentuated role of the organic spacer (3AMP vs 4AMP) over the impact of the perovskitizer (FA vs MA), with the large organic spacer causing a much larger change in the unit cell. The nature of the spacer cations influences the interlayer separation by anchoring deeper or shallower in the "pockets" of the inorganic framework surfaces. On the contrary, the perovskitizer sits within the relatively tight inorganic cage, which can only deform within shorter bounds and therefore the effect is less prominent.

To take a closer look at the role of the organic spacers and perovskitizer in the lattice, we determined the crystal structures of the nine new compounds (Figure 3). Because of the asymmetry of the organic cations, all structures were refined in non-centrosymmetric monoclinic space groups (*Cm*, *Pc* or *Cc*), as justified previously.[65] The refinement details are provided in Table 1 and 2. According to their structural distortion, the inorganic [Pb_2Br_7] framework can be divided into three different modes that originate from the parent compounds 3M A, 3FA, 4MA and 4FA. The three compounds (3MA, 3FAMA and 3FA) in the left column belong to the least distorted mode (mode α). 34MA and 4MA (top row middle and right) are heavily distorted and together belong to the same mode (mode β) that has the perovskite octahedra connecting out-of-phase along the long axis, so that Br anions do not overlap with each other in parallel projection view. The remaining four compounds (34FAMA, 4FAMA, 34FA and 4FA) share another structural mode (mode γ), that has the octahedra tilting in-phase resulting in an eclipsed overlap of the Br anions in parallel projection view.

Compared to the common single-layered perovskite structure where the Pb-X-Pb angles distort parallel to the layer (horizontal tilt), in thicker 2D perovskites the Pb-X-Pb angles perpendicular to the layer (axial tilt) also become relevant. These independent values are illustrated in Figure 3 and are tabulated in order of increasing distortion in Table 3. Bases on this analysis, we were able to quantify the imposed distortion induced by the organic cations to the inorganic lattice. The two clear-cut trends observed relate to the content of 4AMP, for which the Pb-Br-Pb angle decreases as 4AMP incorporation increases. On the antipode, the addition of FA

Accepted Manuscript

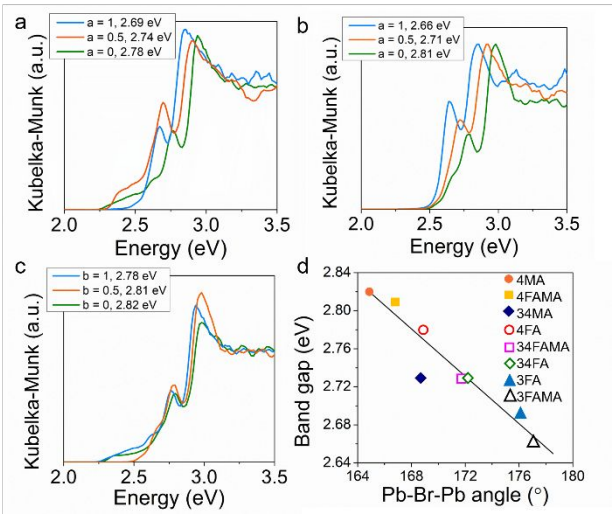

Figure 4. Optical absorption spectra of (a) $(3AMP)_a(4AMP)_{1-a}(FA)Pb_2Br_7$ (a = 0, 0.5, 1); (b) $(3AMP)_a(4AMP)_{1-a}(FA)_{0.5}(MA)_{0.5}Pb_2Br_7$ (a = 0, 0.5, 1); (c) $(4AMP)(FA)_b(MA)_{1-b}Pb_2Br_7$ (b = 0, 0.5, 1). (d) Correlation between the Pb-Br-Pb angle and band gap. The black line is for guidance of the eyes.

is also very clear. Irrespective of whether the system contains 3AMP or 4AMP, the averaged Pb-Br-Pb angle increases with increasing amounts of FA.

Optical absorption. The variation of templating cation within the system and the accumulated structural distortions affect the band gap much more than changing the perovskitizer. This is clearly demonstrated in the optical absorption of the $(3AMP)_a(4AMP)_{1-a}(FA)Pb_2Br_7$ and $(3AMP)_a(4AMP)_{1-a}(FA)_{0.5}(MA)_{0.5}Pb_2Br_7$ series. When changing the composition of 3AMP vs. 4AMP with a fixed perovskitizer (Figure 4a, b), the band gap changes significantly, up to 0.15 eV between 3FAMA and 4FAMA. On the other hand, in the $(4AMP)(FA)_b(MA)_{1-b}Pb_2Br_7$ system, in which the perovskitizer ratio MA/FA varies, the band gap changes only marginally (0.04 eV) from 2.82 eV to 2.78 eV. In terms of the ability in affecting the band gap energy, the spacing cations (3AMP and 4AMP) have stronger effect (~0.15 eV) than the perovskitizers (MA and FA, ~0.04eV) in the current bilayer system as demonstrated above.

The band gap of these materials follows a general trend that, the larger the Pb-Br-Pb angle (less distorted), the smaller the band gap, Figure 4d.[73] Increasing Pb-Br-Pb angle results in a higher degree of overlapping Pb s and Br p orbitals, which leads to strengthening of both bonding and antibonding interactions that broadens the band width and raises the energy level of the valence band maximum (VBM), see discussion below.[74]

Raman and PL spectroscopy. The room temperature low frequency Raman spectra of this set of compounds show broad poorly resolved peaks resolution, which are similar to the previously reported 2D hybrid bi-layered lead iodides[42] as well as to the 3D systems $MAPbBr_3$ and $CsPbBr_3$.[75] $(3AMP)(FA)Pb_2Br_7$ has the highest resolved spectrum of the series, where a series of peaks showing up ~40 cm^{-1}, ~60 cm^{-1} and ~70 cm^{-1}, which could be corresponding to the bending modes of Br-Pb-Br. The mixing of spacing and perovskitizer makes the spectra much less resolved and much broader than the ones with no mixing (4MA, 4FA and 3FA), indicating a more dynamically disordered environment for the solid solution compounds (4FAMA, 3FAMA, 34MA, 34FA and 34FAMA). Interestingly, hybrid lead bromide compounds with lower dimensionalities and non-perovskitic structures have much better resolved Raman peaks than the 2D and 3D materials.[45] The broader shapes of the Raman spectra at these very low frequencies are more characteristic of fluid materials rather than crystalline. They suggest that these 2D bromide perovskites are highly dynamic and disordered on the Raman spectroscopy timescale. This property, is believed to be critical in defining the longer charge transport lifetimes and defect tolerant behavior of perovskites and arises mainly from the inorganic framework's high flexibility which is created by the motions of Pb-Br-Pb angles and the stereochemically active nature of the $6s^2$ lone pair of electrons in the Pb^{2+} centers.[76]

The PL emission energy varies from 2.30 to 2.48 eV (Figure 5b), comparable to a previously reported two-layered lead bromide compound $(BA)_2(FA)Pb_2Br_7$ (2.35 eV).[67] The relatively narrow PL emission feature indicates the nature of the emission comes from free exciton

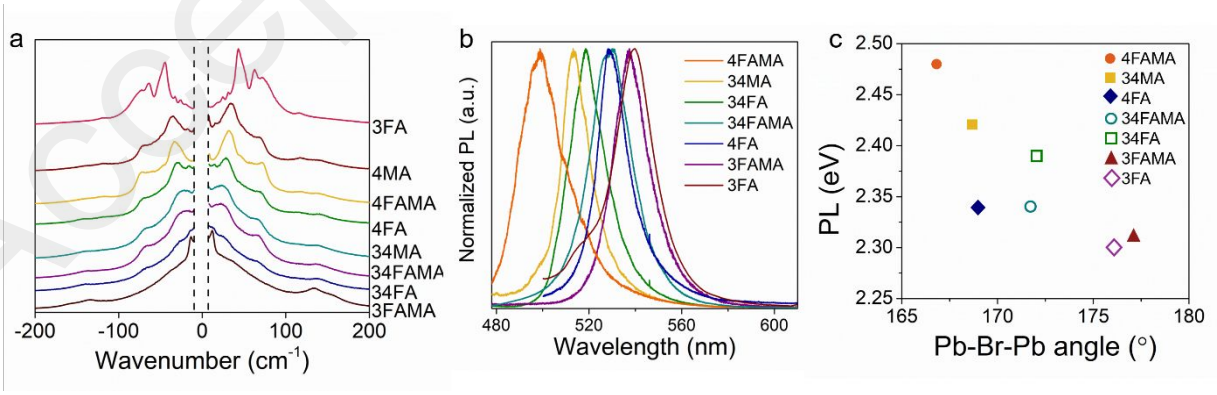

Figure 5. (a) Room-temperature Raman spectra of hybrid lead bromide crystals. The spectral region between ±8 cm^{-1} has been deleted because of the use of notch filter. The spectra were collected using 473 nm laser under ambient condition. (b) Steady-state PL spectra. (c) The PL emission energy shows a similar trend as the band gap, where with increasing Pb-Br-Pb angle the emission energy decreases. 4FA and 34FAMA are a bit off from the trend, which have lower emission energy than expected.

recombination. Averaged PL decay lifetimes of representative compounds are ~2ns, fitted with a biexponential function (Figure S3). We summarize the corresponding PL emission energy with the Pb-Br-Pb angle, and find a similar trend with the band gap evolution with the angle, as shown in Figure 5c. With a larger averaged Pb-Br-Pb angle, the PL emission energy is gradually decreasing.

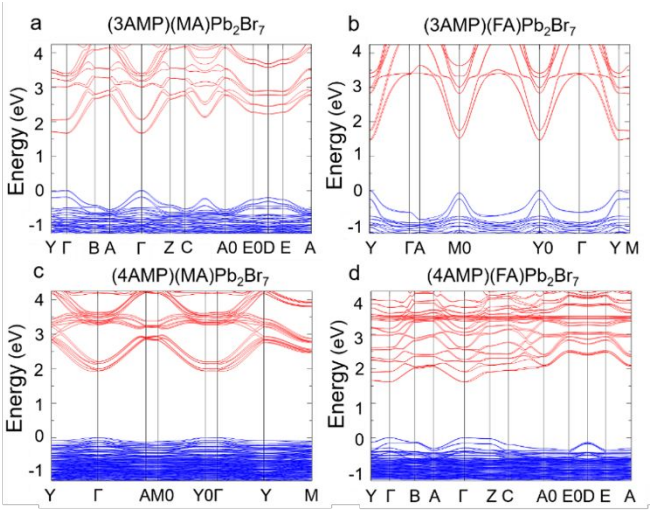

Figure 6. Calculated band structure and band gap of (a) $(3AMP)(MA)Pb_2Br_7$-1.66 eV (at Γ), (b) $(3AMP)(FA)Pb_2Br_7$-1.46 eV (at Y), (c) $(4AMP)(MA)Pb_2Br_7$-1.92 eV (at Γ) and (d) $(4AMP)(FA)Pb_2Br_7$-1.62 eV (at Γ).

Electronic structure calculation. The electronic structures of the original parent compounds $(3AMP)(MA)Pb_2Br_7$, $(3AMP)(FA)Pb_2Br_7$, $(4AMP)(MA)Pb_2Br_7$ and $(4AMP)(FA)Pb_2Br_7$ were calculated based on density functional theory (DFT, including spin-orbit coupling). All compounds are direct band gap semiconductors with calculated band gaps ranging from 1.46 eV to 1.92 eV. The trend in energy gap agrees with the experimental observations that the 3AMPs have smaller band gap than the 4AMPs. Also in agreement with the experiment, for a given spacer cation, the FA compound has smaller band gap than the MA one, see Figure 6. It is also evident that the FA-based compounds have more dispersed valence bands than the MA-based compounds, indicating potentially higher hole mobility. The calculated bandwidths of these materials are quite different, where $(3AMP)(FA)Pb_2Br_7$ shows a wide bandwidth in the conduction bands (~2 eV), in contrast to the shallower conduction bandwidth in $(4AMP)(FA)Pb_2Br_7$ (~0.5 eV). The difference in the bandwidth of the valence band is also noticeable, where $(3AMP)(FA)Pb_2Br_7$ is about 0.8 eV and $(4AMP)(FA)Pb_2Br_7$ (~0.3 eV).

The MA-based compounds $(3AMP)(MA)Pb_2Br_7$ and $(4AMP)(MA)Pb_2Br_7$ have similar bandwidths in the conduction bands, which are around 1 eV. $(3AMP)(MA)Pb_2Br_7$ has much wider conduction bands (~0.5 eV) compared with $(4AMP)(MA)Pb_2Br_7$ (flat and almost no dispersion). The broadest bandwidth in $(3AMP)(FA)Pb_2Br_7$ corresponds to the smallest distortion (largest Pb-Br-Pb angles) amongst all, showing a dependence of the electronic properties on the structural characteristics.

CONCLUSIONS

The successful organic cation alloying on both the spacer interlayer sites and intralayer cage site in the 2D JD type bromide perovskites enable the in depth study of how distortions in the inorganic framework affect key optical properties. The size similarity of the 3AMP and 4AMP cations enable the stabilization of the full range of solid solutions of $(3AMP)_{0.5}(4AMP)_{0.5}(FA)_{0.5}(MA)_{0.5}Pb_2Br_7$. The dual alloying strategy in both the A' and A cation sites produced nine new bi-layered hybrid Dion-Jacobson lead bromide perovskites. The effects of the organic spacer and perovskitizer are observed in the distortion of the $[Pb_2Br_7]$ framework, which three different conformation modes are clearly shown. With the aid of single-crystal X-ray diffraction, we have determined an underlying structural trend, which indicates that upon addition of 4AMP the Pb-Br-Pb angles tend to decrease whereas addition of FA tends to increase the Pb-Br-Pb angles. The distortion of Pb-Br-Pb angles is directly linked to the optical properties of these materials, as the higher the Pb-Br-Pb angles, the lower the band gaps and PL emission energies. Raman spectroscopy indicates the local distortion level of $[Pb_2Br_7]$ increases with higher complexity of the cation compositions. The ability to tune the semiconducting properties by altering the stereochemistry of organic spacers within a simple hybrid perovskite platform further improves our understanding of structure-property relationships, providing a powerful design tool towards property optimization and device engineering.

Methods

Materials. $PbBr_2$ (98%), 3-(aminomethyl)piperidine (Aldrich^{CPR}), 4-(aminomethyl)piperidine (96%), methylammonium chloride (≥98%), formamidine acetate (99%), hydrobromic acid (ACS reagent, 48%) were purchased from Sigma-Aldrich and used as received.

Synthesis of $(A')(A)Pb_2Br_7$ (A' = 3AMP or 4AMP, A = MA or FA). Taking the synthesis of $(3AMP)(FA)Pb_2Br_7$ as an example, an amount of 1.10 g (3 mmol) of $PbBr_2$ was dissolved in 5 mL of HBr (vial A). 312 mg (3 mmol) of formamidinium acetate was added into the previous solution after all $PbBr_2$ was dissolved. In a separate vial (vial B), 1 mL HBr was added into 57 mg (0.5 mmol) of 3- (aminomethyl)piperidine. Under heating and stirring to boil, vial B was poured into vial A and the reaction continued for another 5-10 min until the solution became clear. Plate-like yellow crystals precipitated during slow cooling to room temperature. Yield 372 mg (21.8% based on total Pb content). This procedure applies to the rest of the compounds, except the amount of the cations changes to the ratio shown in Table S11. Only a small amount of single crystals of $(3AMP)(MA)Pb_2Br_7$ could be obtained because of the tendency of the material to decompose.

Single Crystal X-ray Diffraction. Full sphere data were collected after screening for a few frames using either a STOE IPDS 2 or IPDS 2T diffractometer with graphite-monochromatized Mo Kα radiation (λ = 0.71073 Å) (50 kV/40 mA) under N_2 at 293K ($(3AMP)(MA)Pb_2Br_7$, $(3AMP)(FA)Pb_2Br_7$, $(4AMP)(MA)Pb_2Br_7$ and $(4AMP)(FA)Pb_2Br_7$). The collected data was integrated and applied with numerical absorption corrections using the

STOE X-AREA programs. The rest of the compounds were collected using a Bruker Molly instrument with MoKα IμS microfocus source (λ = 0.71073 Å) with MX Optics at 293K. The collected data was integrated and applied with numerical absorption corrections using the APEX3 software. Crystal structures were solved by direct methods and refined by full-matrix least-squares on F^2 using the OLEX2 program package.[77] Note that for the solid solution structures with mixed 3AMP/4AMP or MA/FA, the A' cation was refined as 4AMP and A cation as MA. The actual ratio was given in Table S11 measured by NMR. In the case of $(3AMP)(FA)_{0.5}(MA)_{0.5}Pb_2Br_7$, the cation is disordered and cannot be fully resolved.

Steady-state Photoluminescence. Steady-state PL spectra were collected using HORIBA LabRAM HR Evolution Confocal RAMAN microscope. 473 nm laser (25mW, 0.1% power) was used to excite all samples at 10× or 50× magnification (2μm beam size).

Computational details. First-principles calculations are based on density functional theory (DFT) as implemented in the SIESTA package.[1,2] Experimental structures are used for the inorganic skeleton, well characterized by X-ray diffraction. By contrast, the atomic positions of organic cations have been optimized using the non-local van der Waals density functional of Dion *et al.* corrected by Cooper (C09).[3,4] Spin-orbit coupling is taken into account through the on-site approximation as proposed by Fernández-Seivane *et al.*[5] To prevent conflicts between the on-site treatment and the non-locality of C09, single points calculations are conducted with the revPBE functional on which C09 is based.[6] Core electrons are described with Troullier-Martins pseudopotentials.[7] The valence wavefunctions are developed over double-ζ polarized basis set of finite-range numerical pseudoatomic orbitals.[8] In all cases, an energy cutoff of 150 Ry for real-space mesh size has been used.

ASSOCIATED CONTENT

Supporting Information

Additional crystallographic details (CIF), time-resolved PL, ^1H NMR spectra and photo-response of selected compounds (PDF). This material is available free of charge via the Internet at http://pubs.acs.org.

AUTHOR INFORMATION

Corresponding Author

*m-kanatzidis@northwestern.edu
*cstoumpos@materials.uoc.gr

ACKNOWLEDGMENT

This work was supported by the Department of Energy, Office of Science, Basic Energy Sciences, under Grant SC0012541 (synthesis and structural characterization of materials, M.G.K.). This work was performed, in part, at the Center for Nanoscale Materials, a U.S. Department of Energy Office of Science User Facility, and supported by the U.S. Department of Energy, Office of Science, under Contract No. DE-AC02-06CH11357. This research used resources of the Advanced Photon Source, a U.S. Department of Energy (DOE) Office of Science User Facility operated for the DOE Office of Science by Argonne National Laboratory under Contract No. DE-AC02-06CH11357. Raman measurements were performed at GeoSoilEnviroCARS (The University of Chicago, Sector 13), Advanced Photon Source (APS), Argonne National Laboratory. GeoSoilEnviroCARS is supported by the National Science Foundation–Earth Sciences (EAR-1634415). The Raman system acquisition was supported by the NSF MRI proposal (EAR-1531583). The work at FOTON was performed using HPC resources from GENCI-TGCC/ CINES (Grant 2017-0906724). This work made use of the IMSERC at Northwestern University, which has received support from the Soft and Hybrid Nanotechnology Experimental (SHyNE) Resource (NSF ECCS-1542205), the State of Illinois, and the International Institute for Nanotechnology (IIN).

REFERENCES

(1) Stranks, S. D.; Snaith, H. J. Metal-halide perovskites for photovoltaic and light-emitting devices. *Nat. Nanotechnol.* **2015**, *10*, 391-402.

(2) Stoumpos, C. C.; Kanatzidis, M. G. The Renaissance of Halide Perovskites and Their Evolution as Emerging Semiconductors. *Acc. Chem. Res.* **2015**, *48*, 2791-2802.

(3) Park, N.-G.; Grätzel, M.; Miyasaka, T.; Zhu, K.; Emery, K. Towards stable and commercially available perovskite solar cells. *Nat. Energy* **2016**, *1*, 16152.

(4) Jena, A. K.; Kulkarni, A.; Miyasaka, T. Halide Perovskite Photovoltaics: Background, Status, and Future Prospects. *Chem. Rev.* **2019**, *119*, 3036-3103.

(5) NREL's "Best Research-Cell Efficiencies" Chart. https://www.nrel.gov/pv/assets/pdfs/pv-efficiencies-07-17-2018.pdf

(6) Bailie, C. D.; McGehee, M. D. High-efficiency tandem perovskite solar cells. *MRS Bulletin* **2015**, *40*, 681-686.

(7) McMeekin, D. P.; Sadoughi, G.; Rehman, W.; Eperon, G. E.; Saliba, M.; Hörantner, M. T.; Haghighirad, A.; Sakai, N.; Korte, L.; Rech, B.; Johnston, M. B.; Herz, L. M.; Snaith, H. J. A mixed-cation lead mixed-halide perovskite absorber for tandem solar cells. *Science* **2016**, *351*, 151-155.

(8) Meng, L.; Yao, E.-P.; Hong, Z.; Chen, H.; Sun, P.; Yang, Z.; Li, G.; Yang, Y. Pure Formamidinium-Based Perovskite Light-Emitting Diodes with High Efficiency and Low Driving Voltage. *Adv. Mater.* **2017**, *29*, 1603826.

(9) Yang, X.; Zhang, X.; Deng, J.; Chu, Z.; Jiang, Q.; Meng, J.; Wang, P.; Zhang, L.; Yin, Z.; You, J. Efficient green light-emitting diodes based on quasi-two-dimensional composition and phase engineered perovskite with surface passivation. *Nat. Commun.* **2018**, *9*, 570.

(10) Cho, H.; Jeong, S.-H.; Park, M.-H.; Kim, Y.-H.; Wolf, C.; Lee, C.-L.; Heo, J. H.; Sadhanala, A.; Myoung, N.; Yoo, S.; Im, S. H.; Friend, R. H.; Lee, T.-W. Overcoming the electroluminescence efficiency limitations of perovskite light-emitting diodes. *Science* **2015**, *350*, 1222-1225.

(11) Quan, L. N.; Zhao, Y.; García de Arquer, F. P.; Sabatini, R.; Walters, G.; Voznyy, O.; Comin, R.; Li, Y.; Fan, J. Z.; Tan, H.; Pan, J.; Yuan, M.; Bakr, O. M.; Lu, Z.; Kim, D. H.; Sargent, E. H. Tailoring the Energy Landscape in Quasi-2D

Accepted Manuscript

Halide Perovskites Enables Efficient Green-Light Emission. *Nano Lett.* **2017**, *17*, 3701-3709.

(12) Quan, L. N.; García de Arquer, F. P.; Sabatini, R. P.; Sargent, E. H. Perovskites for Light Emission. *Adv. Mater.* **2018**, *30*, 1801996.

(13) Cao, Y.; Wang, N.; Tian, H.; Guo, J.; Wei, Y.; Chen, H.; Miao, Y.; Zou, W.; Pan, K.; He, Y.; Cao, H.; Ke, Y.; Xu, M.; Wang, Y.; Yang, M.; Du, K.; Fu, Z.; Kong, D.; Dai, D.; Jin, Y.; Li, G.; Li, H.; Peng, Q.; Wang, J.; Huang, W. Perovskite light-emitting diodes based on spontaneously formed submicrometre-scale structures. *Nature* **2018**, *562*, 249-253.

(14) Saliba, M.; Matsui, T.; Domanski, K.; Seo, J.-Y.; Ummadisingu, A.; Zakeeruddin, S. M.; Correa-Baena, J.-P.; Tress, W. R.; Abate, A.; Hagfeldt, A.; Grätzel, M. Incorporation of rubidium cations into perovskite solar cells improves photovoltaic performance. *Science* **2016**, *354*, 206-209.

(15) Saliba, M.; Matsui, T.; Seo, J.-Y.; Domanski, K.; Correa-Baena, J.-P.; Nazeeruddin, M. K.; Zakeeruddin, S. M.; Tress, W.; Abate, A.; Hagfeldt, A.; Grätzel, M. Cesium-containing triple cation perovskite solar cells: improved stability, reproducibility and high efficiency. *Energy Environ. Sci.* **2016**, *9*, 1989-1997.

(16) Jeon, N. J.; Noh, J. H.; Yang, W. S.; Kim, Y. C.; Ryu, S.; Seo, J.; Seok, S. I. Compositional engineering of perovskite materials for high-performance solar cells. *Nature* **2015**, *517*, 476.

(17) Rehman, W.; McMeekin, D. P.; Patel, J. B.; Milot, R. L.; Johnston, M. B.; Snaith, H. J.; Herz, L. M. Photovoltaic mixed-cation lead mixed-halide perovskites: links between crystallinity, photo-stability and electronic properties. *Energy Environ. Sci.* **2017**, *10*, 361-369.

(18) Ke, W.; Xiao, C.; Wang, C.; Saparov, B.; Duan, H.-S.; Zhao, D.; Xiao, Z.; Schulz, P.; Harvey, S. P.; Liao, W.; Meng, W.; Yu, Y.; Cimaroli, A. J.; Jiang, C.-S.; Zhu, K.; Al-Jassim, M.; Fang, G.; Mitzi, D. B.; Yan, Y. Employing Lead Thiocyanate Additive to Reduce the Hysteresis and Boost the Fill Factor of Planar Perovskite Solar Cells. *Adv. Mater.* **2016**, *28*, 5214-5221.

(19) Li, X.; Dar, M. I.; Yi, C.; Luo, J.; Tschumi, M.; Zakeeruddin, S. M.; Nazeeruddin, M. K.; Han, H.; Grätzel, M. Improved performance and stability of perovskite solar cells by crystal crosslinking with alkylphosphonic acid ω-ammonium chlorides. *Nat. Chem.* **2015**, *7*, 703-711.

(20) Mei, A.; Li, X.; Liu, L.; Ku, Z.; Liu, T.; Rong, Y.; Xu, M.; Hu, M.; Chen, J.; Yang, Y.; Grätzel, M.; Han, H. A hole-conductor–free, fully printable mesoscopic perovskite solar cell with high stability. *Science* **2014**, *345*, 295-298.

(21) Poglitsch, A.; Weber, D. Dynamic disorder in methylammoniumtrihalogenoplumbates (II) observed by millimeter - wave spectroscopy. *J. Chem. Phys.* **1987**, *87*, 6373-6378.

(22) Yaffe, O.; Guo, Y.; Tan, L. Z.; Egger, D. A.; Hull, T.; Stoumpos, C. C.; Zheng, F.; Heinz, T. F.; Kronik, L.; Kanatzidis, M. G.; Owen, J. S.; Rappe, A. M.; Pimenta, M. A.; Brus, L. E. Local Polar Fluctuations in Lead Halide Perovskite Crystals. *Phys. Rev. Lett.* **2017**, *118*, 136001.

(23) Fabini, D. H.; Laurita, G.; Bechtel, J. S.; Stoumpos, C. C.; Evans, H. A.; Kontos, A. G.; Raptis, Y. S.; Falaras, P.; Van der Ven, A.; Kanatzidis, M. G.; Seshadri, R. Dynamic Stereochemical Activity of the Sn^{2+} Lone Pair in Perovskite CsSnBr3. *J. Am. Chem. Soc.* **2016**, *138*, 11820-11832.

(24) Cao, D. H.; Stoumpos, C. C.; Farha, O. K.; Hupp, J. T.; Kanatzidis, M. G. 2D Homologous Perovskites as Light-Absorbing Materials for Solar Cell Applications. *J. Am. Chem. Soc.* **2015**, *137*, 7843-7850.

(25) Smith, I. C.; Hoke, E. T.; Solis-Ibarra, D.; McGehee, M. D.; Karunadasa, H. I. A Layered Hybrid Perovskite Solar-Cell Absorber with Enhanced Moisture Stability. *Angew. Chem. Int. Ed.* **2014**, *53*, 11232-11235.

(26) Quan, L. N.; Yuan, M.; Comin, R.; Voznyy, O.; Beauregard, E. M.; Hoogland, S.; Buin, A.; Kirmani, A. R.; Zhao, K.; Amassian, A.; Kim, D. H.; Sargent, E. H. Ligand-Stabilized Reduced-Dimensionality Perovskites. *J. Am. Chem. Soc.* **2016**, *138*, 2649-2655.

(27) Tsai, H.; Nie, W.; Blancon, J.-C.; Stoumpos, C. C.; Asadpour, R.; Harutyunyan, B.; Neukirch, A. J.; Verduzco, R.; Crochet, J. J.; Tretiak, S.; Pedesseau, L.; Even, J.; Alam, M. A.; Gupta, G.; Lou, J.; Ajayan, P. M.; Bedzyk, M. J.; Kanatzidis, M. G.; Mohite, A. D. High-efficiency two-dimensional Ruddlesden–Popper perovskite solar cells. *Nature* **2016**, *536*, 312-316.

(28) Mao, L.; Wu, Y.; Stoumpos, C. C.; Traore, B.; Katan, C.; Even, J.; Wasielewski, M. R.; Kanatzidis, M. G. Tunable White-Light Emission in Single-Cation-Templated Three-Layered 2D Perovskites $(CH_3CH_2NH_3)_4Pb_3Br_{10-x}Cl_x$. *J. Am. Chem. Soc.* **2017**, *139*, 11956-11963.

(29) Mao, L.; Stoumpos, C. C.; Kanatzidis, M. G. Two-Dimensional Hybrid Halide Perovskites: Principles and Promises. *J. Am. Chem. Soc.* **2018**, *141*, 1171-1190.

(30) Smith, M. D.; Crace, E. J.; Jaffe, A.; Karunadasa, H. I. The Diversity of Layered Halide Perovskites. *Annu. Rev. Mater. Res.* **2018**, *48*, 111-136.

(31) Guo, P.; Stoumpos, C. C.; Mao, L.; Sadasivam, S.; Ketterson, J. B.; Darancet, P.; Kanatzidis, M. G.; Schaller, R. D. Cross-plane coherent acoustic phonons in two-dimensional organic-inorganic hybrid perovskites. *Nat. Commun.* **2018**, *9*, 2019.

(32) Blancon, J. C.; Stier, A. V.; Tsai, H.; Nie, W.; Stoumpos, C. C.; Traoré, B.; Pedesseau, L.; Kepenekian, M.; Katsutani, F.; Noe, G. T.; Kono, J.; Tretiak, S.; Crooker, S. A.; Katan, C.; Kanatzidis, M. G.; Crochet, J. J.; Even, J.; Mohite, A. D. Scaling law for excitons in 2D perovskite quantum wells. *Nat. Commun.* **2018**, *9*, 2254.

(33) Straus, D. B.; Kagan, C. R. Electrons, Excitons, and Phonons in Two-Dimensional Hybrid Perovskites: Connecting Structural, Optical, and Electronic Properties. *J. Phys. Chem. Lett.* **2018**, *9*, 1434-1447.

(34) Zhai, Y.; Baniya, S.; Zhang, C.; Li, J.; Haney, P.; Sheng, C.-X.; Ehrenfreund, E.; Vardeny, Z. V. Giant Rashba splitting in 2D organic-inorganic halide perovskites measured by transient spectroscopies. *Sci. Adv.* **2017**, *3*, e1700704.

(35) Lu, H.; Wang, J.; Xiao, C.; Pan, X.; Chen, X.; Brunecky, R.; Berry, J. J.; Zhu, K.; Beard, M. C.; Vardeny, Z. V. Spin-dependent charge transport through 2D chiral hybrid lead-iodide perovskites. *Sci. Adv.* **2019**, *5*, eaay0571.

(36) Liao, K.; Hu, X.; Cheng, Y.; Yu, Z.; Xue, Y.; Chen, Y.; Gong, Q. Spintronics of Hybrid Organic–Inorganic Perovskites: Miraculous Basis of Integrated Optoelectronic Devices. *Adv. Opt. Mater.* **2019**, *7*, 1900350.

(37) Zhang, F.; Lu, H.; Tong, J.; Berry, J. J.; Beard, M. C.; Zhu, K. Advances in two-dimensional organic–inorganic hybrid perovskites. *Energy Environ Sci.* **2020**.

ACS Paragon Plus Environment

(38) Kieslich, G.; Sun, S.; Cheetham, A. K. Solid-state principles applied to organic-inorganic perovskites: new tricks for an old dog. *Chem. Sci.* **2014**, *5*, 4712-4715.

(39) Kieslich, G.; Sun, S.; Cheetham, A. K. An extended tolerance factor approach for organic–inorganic perovskites. *Chem. Sci.* **2015**, *6*, 3430-3433.

(40) Fu, Y.; Jiang, X.; Li, X.; Traore, B.; Spanopoulos, I.; Katan, C.; Even, J.; Kanatzidis, M. G.; Harel, E. Cation Engineering in Two-Dimensional Ruddlesden–Popper Lead Iodide Perovskites with Mixed Large A-Site Cations in the Cages. *J. Am. Chem. Soc.* **2020**, *142*, 4008-4021.

(41) Stoumpos, C. C.; Mao, L.; Malliakas, C. D.; Kanatzidis, M. G. Structure–Band Gap Relationships in Hexagonal Polytypes and Low-Dimensional Structures of Hybrid Tin Iodide Perovskites. *Inorg. Chem.* **2017**, *56*, 56-73.

(42) Fu, Y.; Hautzinger, M. P.; Luo, Z.; Wang, F.; Pan, D.; Aristov, M. M.; Guzei, I. A.; Pan, A.; Zhu, X.; Jin, S. Incorporating Large A Cations into Lead Iodide Perovskite Cages: Relaxed Goldschmidt Tolerance Factor and Impact on Exciton–Phonon Interaction. *ACS Cent. Sci* **2019**, *5*, 1377-1386.

(43) Saparov, B.; Mitzi, D. B. Organic–Inorganic Perovskites: Structural Versatility for Functional Materials Design. *Chem. Rev.* **2016**, *116*, 4558-4596.

(44) Passarelli, J. V.; Fairfield, D. J.; Sather, N. A.; Hendricks, M. P.; Sai, H.; Stern, C. L.; Stupp, S. I. Enhanced Out-of-Plane Conductivity and Photovoltaic Performance in n = 1 Layered Perovskites through Organic Cation Design. *J. Am. Chem. Soc.* **2018**, *140*, 7313-7323.

(45) Mao, L.; Guo, P.; Kepenekian, M.; Hadar, I.; Katan, C.; Even, J.; Schaller, R. D.; Stoumpos, C. C.; Kanatzidis, M. G. Structural Diversity in White-light Emitting Hybrid Lead Bromide Perovskites. *J. Am. Chem. Soc.* **2018**, *140*, 13078-13088.

(46) Mitzi, D. B.; Medeiros, D. R.; Malenfant, P. R. L. Intercalated Organic–Inorganic Perovskites Stabilized by Fluoroaryl–Aryl Interactions. *Inorg. Chem.* **2002**, *41*, 2134-2145.

(47) Mercier, N. $(HO_2C(CH_2)_3NH_3)_2(CH_3NH_3)Pb_2I_7$: a predicted non-centrosymmetrical structure built up from carboxylic acid supramolecular synthons and bilayer perovskite sheets. *CrystEngComm* **2005**, *7*, 429-432.

(48) Solis-Ibarra, D.; Karunadasa, H. I. Reversible and Irreversible Chemisorption in Nonporous-Crystalline Hybrids. *Angew. Chem. Int. Ed.* **2014**, *53*, 1039-1042.

(49) Ortiz-Cervantes, C.; Román-Román, P. I.; Vazquez-Chavez, J.; Hernández-Rodríguez, M.; Solis-Ibarra, D. Thousand-fold Conductivity Increase in 2D Perovskites by Polydiacetylene Incorporation and Doping. *Angew. Chem. Int. Ed.* **2018**, *57*, 13882-13886.

(50) Smith, M. D.; Jaffe, A.; Dohner, E. R.; Lindenberg, A. M.; Karunadasa, H. I. Structural origins of broadband emission from layered Pb-Br hybrid perovskites. *Chem. Sci.* **2017**, *8*, 4497-4504.

(51) Mao, L.; Tsai, H.; Nie, W.; Ma, L.; Im, J.; Stoumpos, C. C.; Malliakas, C. D.; Hao, F.; Wasielewski, M. R.; Mohite, A. D.; Kanatzidis, M. G. Role of Organic Counterion in Lead- and Tin-based Two-dimensional Semiconducting Iodide Perovskites and Application in Planar Solar Cells. *Chem. Mater.* **2016**, *28*, 7781-7792.

(52) Dohner, E. R.; Jaffe, A.; Bradshaw, L. R.; Karunadasa, H. I. Intrinsic White-Light Emission from Layered Hybrid Perovskites. *J. Am. Chem. Soc.* **2014**, *136*, 13154-13157.

(53) Mao, L.; Wu, Y.; Stoumpos, C. C.; Wasielewski, M. R.; Kanatzidis, M. G. White-light Emission and Structural Distortion in New Corrugated 2D Lead Bromide Perovskites. *J. Am. Chem. Soc.* **2017**, *139*, 5210–5215.

(54) Lehner, A. J.; Fabini, D. H.; Evans, H. A.; Hébert, C.-A.; Smock, S. R.; Hu, J.; Wang, H.; Zwanziger, J. W.; Chabinyc, M. L.; Seshadri, R. Crystal and Electronic Structures of Complex Bismuth Iodides A3Bi2I9 (A = K, Rb, Cs) Related to Perovskite: Aiding the Rational Design of Photovoltaics. *Chem. Mater.* **2015**, *27*, 7137-7148.

(55) Chang, J.-H.; Doert, T.; Ruck, M. Structural Variety of Defect Perovskite Variants $M_3E_2X_9$ (M = Rb, Tl, E = Bi, Sb, X = Br, I). *Z. Anorg. Allg. Chem* **2016**, *642*, 736-748.

(56) Stoumpos, C. C.; Soe, C. M. M.; Tsai, H.; Nie, W.; Blancon, J.-C.; Cao, D. H.; Liu, F.; Traoré, B.; Katan, C.; Even, J.; Mohite, A. D.; Kanatzidis, M. G. High Members of the 2D Ruddlesden-Popper Halide Perovskites: Synthesis, Optical Properties, and Solar Cells of $(CH_3(CH_2)_3NH_3)_2(CH_3NH_3)_4Pb_5I_{16}$. *Chem* **2017**, *2*, 427-440.

(57) Soe, C. M. M.; Nagabhushana, G. P.; Shivaramaiah, R.; Tsai, H.; Nie, W.; Blancon, J.-C.; Melkonyan, F.; Cao, D. H.; Traoré, B.; Pedesseau, L.; Kepenekian, M.; Katan, C.; Even, J.; Marks, T. J.; Navrotsky, A.; Mohite, A. D.; Stoumpos, C. C.; Kanatzidis, M. G. Structural and thermodynamic limits of layer thickness in 2D halide perovskites. *Proc. Natl. Acad. Sci.* **2018**, 201811006.

(58) Li, X.; Hoffman, J.; Ke, W.; Chen, M.; Tsai, H.; Nie, W.; Mohite, A. D.; Kepenekian, M.; Katan, C.; Even, J.; Wasielewski, M. R.; Stoumpos, C. C.; Kanatzidis, M. G. Two-dimensional Halide Perovskites Incorporating Straight Chain Symmetric Diammonium Ions, $(NH_3C_mH_{2m}NH_3)(CH_3NH_3)_{n-1}Pb_nI_{3n+1}$ (m = 4 - 9 ; n = 1 - 4). *J. Am. Chem. Soc.* **2018**, *140*, 12226-12238.

(59) Mao, L.; Kennard, R. M.; Traore, B.; Ke, W.; Katan, C.; Even, J.; Chabinyc, M. L.; Stoumpos, C. C.; Kanatzidis, M. G. Seven-Layered 2D Hybrid Lead Iodide Perovskites. *Chem* **2019**, *5*, 2593-2604.

(60) Connor, B. A.; Leppert, L.; Smith, M. D.; Neaton, J. B.; Karunadasa, H. I. Layered Halide Double Perovskites: Dimensional Reduction of Cs2AgBiBr6. *J. Am. Chem. Soc.* **2018**, *140*, 5235-5240.

(61) Jana, M. K.; Janke, S. M.; Dirkes, D. J.; Dovletgeldi, S.; Liu, C.; Qin, X.; Gundogdu, K.; You, W.; Blum, V.; Mitzi, D. B. Direct-Bandgap 2D Silver–Bismuth Iodide Double Perovskite: The Structure-Directing Influence of an Oligothiophene Spacer Cation. *J. Am. Chem. Soc.* **2019**, *141*, 7955-7964.

(62) Bi, L.-Y.; Hu, Y.-Q.; Li, M.-Q.; Hu, T.-L.; Zhang, H.-L.; Yin, X.-T.; Que, W.-X.; Lassoued, M. S.; Zheng, Y.-Z. Two-dimensional lead-free iodide-based hybrid double perovskites: crystal growth, thin-film preparation and photocurrent responses. *J. Mater. Chem. A* **2019**, *7*, 19662-19667.

(63) Mao, L.; Teicher, S. M. L.; Stoumpos, C. C.; Kennard, R. M.; DeCrescent, R. A.; Wu, G.; Schuller, J. A.; Chabinyc, M. L.; Cheetham, A. K.; Seshadri, R. Chemical and Structural Diversity of Hybrid Layered Double Perovskite Halides. *J. Am. Chem. Soc.* **2019**, *141*, 19099-19109.

Accepted Manuscript

(64) Stoumpos, C. C.; Cao, D. H.; Clark, D. J.; Young, J.; Rondinelli, J. M.; Jang, J. I.; Hupp, J. T.; Kanatzidis, M. G. Ruddlesden–Popper Hybrid Lead Iodide Perovskite 2D Homologous Semiconductors. *Chem. Mater.* **2016**, *28*, 2852-2867.

(65) Mao, L.; Ke, W.; Pedesseau, L.; Wu, Y.; Katan, C.; Even, J.; Wasielewski, M. R.; Stoumpos, C. C.; Kanatzidis, M. G. Hybrid Dion–Jacobson 2D Lead Iodide Perovskites. *J. Am. Chem. Soc.* **2018**, *140*, 3775-3783.

(66) Wu, Z.; Ji, C.; Li, L.; Kong, J.; Sun, Z.; Zhao, S.; Wang, S.; Hong, M.; Luo, J. Alloying n-Butylamine into $CsPbBr_3$ To Give a Two-Dimensional Bilayered Perovskite Ferroelectric Material. *Angew. Chem. Int. Ed.* **2018**, 57, 8140-8143.

(67) Li, L.; Shang, X.; Wang, S.; Dong, N.; Ji, C.; Chen, X.; Zhao, S.; Wang, J.; Sun, Z.; Hong, M.; Luo, J. Bilayered Hybrid Perovskite Ferroelectric with Giant Two-Photon Absorption. *J. Am. Chem. Soc.* **2018**, *140*, 6806-6809.

(68) Li, L.; Sun, Z.; Wang, P.; Hu, W.; Wang, S.; Ji, C.; Hong, M.; Luo, J. Tailored Engineering of an Unusual $(C_4H_9NH_3)_2(CH_3NH_3)_2Pb_3Br_{10}$ Two-Dimensional Multilayered Perovskite Ferroelectric for a High-Performance Photodetector. *Angew. Chem. Int. Ed.* **2017**, *56*, 12150-12154.

(69) Li, L.; Liu, X.; Li, Y.; Xu, Z.; Wu, Z.; Han, S.; Tao, K.; Hong, M.; Luo, J.; Sun, Z. Two-Dimensional Hybrid Perovskite-Type Ferroelectric for Highly Polarization-Sensitive Shortwave Photodetection. *J. Am. Chem. Soc.* **2019**, *141*, 2623-2629.

(70) Stoumpos, C. C.; Malliakas, C. D.; Kanatzidis, M. G. Semiconducting Tin and Lead Iodide Perovskites with Organic Cations: Phase Transitions, High Mobilities, and Near-Infrared Photoluminescent Properties. *Inorg. Chem.* **2013**, 52, 9019-9038.

(71) Spanopoulos, I.; Ke, W.; Stoumpos, C. C.; Schueller, E. C.; Kontsevoi, O. Y.; Seshadri, R.; Kanatzidis, M. G. Unraveling the Chemical Nature of the 3D "Hollow" Hybrid Halide Perovskites. *J. Am. Chem. Soc.* **2018**, *140*, 5728-5742.

(72) Note that 34MA is the only compound with a β not equals to ~90, thus the cell is transformed to an β= 90 cell using a matrix (0 -0.5 0.5, 0 0.5 0.5, -0.5 0 -0.5) and the long axis becomes 16.082.

(73) Knutson, J. L.; Martin, J. D.; Mitzi, D. B. Tuning the Band Gap in Hybrid Tin Iodide Perovskite Semiconductors Using Structural Templating. *Inorg. Chem.* **2005**, *44*, 4699-4705.

(74) Liu, G.; Gong, J.; Kong, L.; Schaller, R. D.; Hu, Q.; Liu, Z.; Yan, S.; Yang, W.; Stoumpos, C. C.; Kanatzidis, M. G.; Mao, H.-k.; Xu, T. Isothermal pressure-derived metastable states in 2D hybrid perovskites showing enduring bandgap narrowing. *Proc. Natl. Acad. Sci.* **2018**, *115*, 8076-8081.

(75) Yaffe, O.; Guo, Y.; Tan, L. Z.; Egger, D. A.; Hull, T.; Stoumpos, C. C.; Zheng, F.; Heinz, T. F.; Kronik, L.; Kanatzidis, M. G.; Owen, J. S.; Rappe, A. M.; Pimenta, M. A.; Brus, L. E. Local Polar Fluctuations in Lead Halide Perovskite Crystals. *Physical Review Letters* **2017**, *118*, 136001.

(76) Laurita, G.; Fabini, D. H.; Stoumpos, C. C.; Kanatzidis, M. G.; Seshadri, R. Chemical tuning of dynamic cation off-centering in the cubic phases of hybrid tin and lead halide perovskites. *Chemical Science* **2017**, *8*, 5628-5635.

(77) Dolomanov, O. V.; Bourhis, L. J.; Gildea, R. J.; Howard, J. A.; Puschmann, H. OLEX2: a complete structure solution, refinement and analysis program. *J. Appl. Crystallogr.* **2009**, *42*, 339-341.

TOC graphic

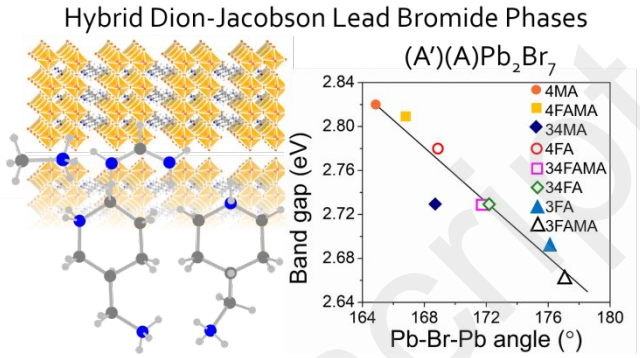

Accepted Manuscript